ACS OMEGA

http://pubs.acs.org/journal/acsodf

Article

Onion-like Carbons Provide a Favorable Electrocatalytic Platform for the Sensitive Detection of Tramadol Drug

Tobechukwu J. Ehirim, Okoroike C. Ozoemena, Patrick V. Mwonga, Aderemi B. Haruna, Thapelo P. Mofokeng, Karolien De Wael, and Kenneth I. Ozoemena*

Cite This: *ACS Omega* 2022, 7, 47892−47905

Read Online

ACCESS | Metrics & More | Article Recommendations

ABSTRACT: This work reports the first study on the possible application of nanodiamond-derived onion-like carbons (OLCs), in comparison with conductive carbon black (CB), as an electrode platform for the electrocatalytic detection of tramadol (an important drug of abuse). The physicochemical properties of OLCs and CB were determined using X-ray diffraction (XRD), Raman, scanning electron microscopy (SEM), Brunauer−Emmett−Teller (BET), and thermogravimetric analysis (TGA). The OLC exhibits, among others, higher surface area, more surface defects, and higher thermal stability than CB. From the electrochemical analysis (interrogated using cyclic voltammetry, differential pulse voltammetry, and electrochemical impedance spectroscopy), it is shown that an OLC-modified glassy carbon electrode (GCE-OLC) allows faster electron transport and electrocatalysis toward tramadol compared to a GCE-CB. To establish the underlying science behind the high performance of the OLC, theoretical calculations (density functional theory (DFT) simulations) were conducted. DFT predicts that OLC allows for weaker surface binding of tramadol (E_{ad} = −26.656 eV) and faster kinetic energy (K.E. = −155.815 Ha) than CB (E_{ad} = −40.174 eV and −305.322 Ha). The GCE-OLC shows a linear calibration curve for tramadol over the range of ∼55 to 392 μM, with high sensitivity (0.0315 μA/μM) and low limit of detection (LoD) and quantification (LoQ) (3.8 and 12.7 μM, respectively). The OLC-modified screen-printed electrode (SPE-OLC) was successfully applied for the sensitive detection of tramadol in real pharmaceutical formulations and human serum. The OLC-based electrochemical sensor promises to be useful for the sensitive and accurate detection of tramadol in clinics, quality control, and routine quantification of tramadol drugs in pharmaceutical formulations.

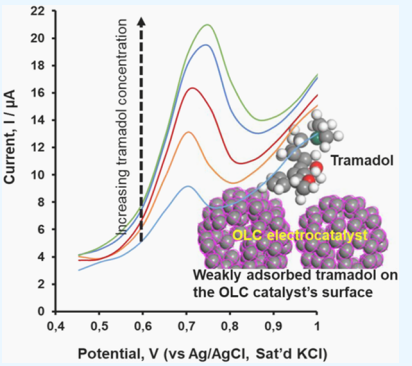

1. INTRODUCTION

The abuse of addiction drugs is one of the major global health challenges, with tramadol (TR) regarded as one of the most abused drugs.[1,2] TR belongs to the phenanthrene opium alkaloids and, albeit being a weak opioid, it is a strong pain reliever and is regularly used in the treatment of moderate to severe pain, especially in postoperative care.[1,3,4] TR hydrochloride is marketed as a racemic mixture of *R*- and *S*-stereoisomers, i.e., (1*RS*,2*RS*)-2-[(dimethylamino)methyl]-1-(3-methoxyphenyl)-cyclohexan-1-ol hydrochloride (Figure 1)[5,6] because the two isomers strongly complement the analgesic properties of each other. Unlike conventional opioid-based analgesics, its mechanism of easing pain is somewhat different: it inhibits the reuptake of norepinephrine and serotonin, thereby increasing their release.[7] TR is an addictive drug that has become a menace in most countries including African countries such as Nigeria, Ghana, etc, leading to a wide ban in African countries.[8,9] TR is regarded as relatively safe when used at the prescribed dosage. However, tramadol overdose or intoxication leads to high levels of tramadol in the blood and serious consequences such as cardiac complications and death.[10,11] In addition, TR is being implicated as an environmental risk,[12−14] especially in urban water pollution. A high concentration of TR is required to

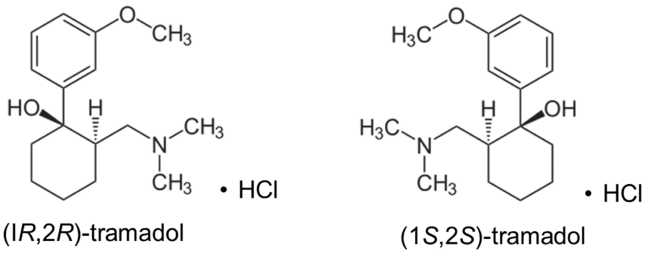

Figure 1. Isomeric structures of commercial tramadol hydrochloride.

Received: September 3, 2022
Accepted: October 17, 2022
Published: December 15, 2022

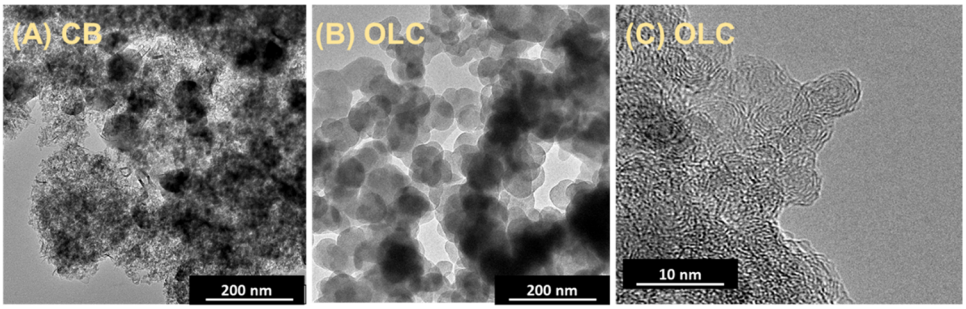

Figure 2. SEM images of (A) CB and (B) OLC and (C) HRTEM image of OLC.

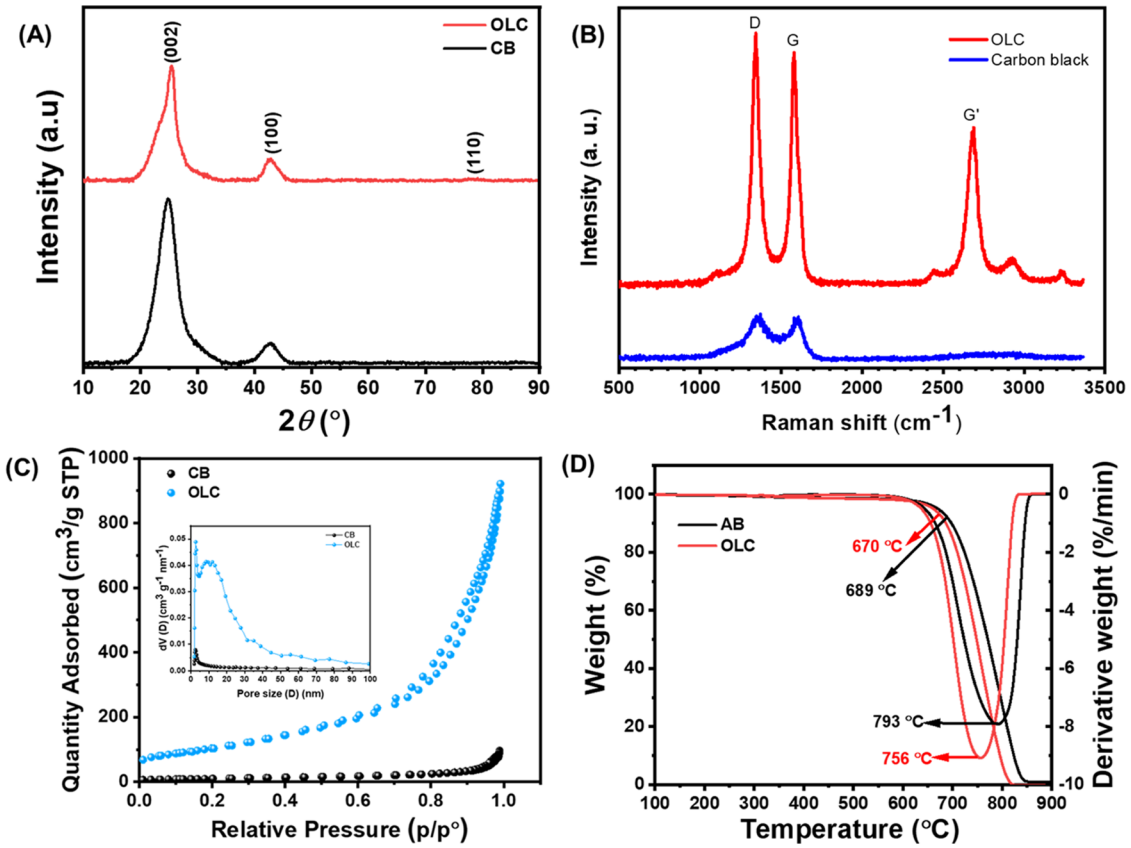

Figure 3. Comparing powder XRD (A), Raman spectra (B), BET adsorption−desorption curve, and (inset) pore size distribution curves (C) and TGA and their corresponding derivative TGA (D) of OLC and CB.

achieve the therapeutic effect in patients. However, only 65−70% of the TR dosage is metabolized and absorbed by the body, while the remaining unmetabolized drug (ca. 35%) is excreted in the urine, which can find its way into the surface and underground water reserves.[12−14]

Based on the above health and environmental challenges of TR, there have been consistent efforts among sensor researchers on developing simpler methods for a rapid, sensitive, and selective detection of TR in its pharmaceutical formulation and human biological samples. The detection of opioids in patients' samples involves the use of standard techniques, notably high-performance liquid chromatography (HPLC),[15] including the HPLC integrated with diode array detectors (HPLC-DADs),[4] or with a mass spectrometer (HPLC-MS),[3,16] solid-state electrochemiluminescence,[17] and solid-phase extraction with UV−vis spectrophotometry.[18] These HPLC-based techniques are bulky and expensive techniques that require a high level of expertise to perform. The need for fast and accurate detection of TR to curb the abuse has necessitated the intense exploration of electrochemical techniques as viable alternatives.[13,19−33] Electrochemical methods are associated with several advantages including low cost, rapidity of detection, simplicity of operation with basic training skills, and ease of miniaturization for point-of-care usage.

To date, carbon-based electrodes remain the most famous sensors for the detection of TR, which includes multiwalled carbon nanotubes (MWCNTs),[24] graphene modified with metal oxide,[21] graphene oxide (GO) integrated with MWCNTs,[28] and carbon nanoparticles (CNPs).[33] These carbon materials have been reported to exhibit different sensitivities for the electrocatalytic detection of TR. However, we are not aware of any report that provides a basic

https://doi.org/10.1021/acsomega.2c05722
ACS Omega 2022, 7, 47892−47905

understanding of the possible reasons for the differences in the sensitivities.

In this work, we investigate the application of onion-like carbon (OLC) as an electrocatalyst for tramadol and compare its performance with a well-known conductive carbon black (CB) (i.e., Super C45). In 2002, Keller et al.[34] reported the first use of OLC as a catalyst for the synthesis of styrene. There are few reports on the use of OLC in electrochemistry, especially in the field of energy storage,[35−39] but its use in electrocatalysis has rarely been explored.[40−43] This work shows that OLC is a viable carbon catalyst for tramadol detection compared to the CB counterpart. Preliminary theoretical insights (DFT calculations) predict that the possible reason for the high electrocatalytic performance of the OLC is that the adsorption energy of tramadol onto the surface of OLC is weaker than on the surface of CB.

2. RESULTS AND DISCUSSION

2.1. Material Characterization. Figure 2 shows the SEM images of CB and OLC and the HRTEM image of the OLC. The SEM images show that CB comprises impure carbonaceous materials, while the OLC is of high purity. The HRTEM images of the OLC clearly confirm its characteristic graphic concentric rings.[39]

Figure 3 compares the XRD patterns (Figure 3A) and Raman spectra (Figure 3B) of the two carbon materials. The XRD patterns (Figure 3A) show a broad diffraction peak centered at $2\theta = 25°$ and a small diffraction peak at $2\theta = 3.2°$, both of which are related to the (002) and (101) diffraction patterns of the disordered carbon structure.[44] Structural information of CB and OLC was obtained with Raman spectroscopy (Figure 3B).

The D band observed around the wavelength of 1350 cm^{-1} is due to the vibrations arising from the defect/disorder/amorphous carbon atoms (sp^2-hybridized), while the G band observed around 1580 cm^{-1} is ascribed to the ordered/crystalline graphitic carbon atoms (sp^3-hybridized). The G′ band observed at around wavelength 2700 cm^{-1} is due to the process of two-photon elastic scattering. The intensity ratio of the D and G bands (I_D/I_G) is used to determine the extent of defects or graphitization present in the carbon materials; the higher the ratio, the higher the defects (lesser the graphitization). In addition, the higher the ratio of the $I_{G'}/I_G$, the higher the purity of the carbon.[45−47] The I_D/I_G values were estimated to be 1.06 and 1.04 for the OLC and CB, respectively, meaning that OLC is slightly more defective than CB. The $I_{G'}/I_G$ ratio for OLC was 0.76, while that for CB was zero, suggesting that OLC is of high purity, while CB is mostly of poor quality. The porosity of CB and OLC was studied using N_2 adsorption−desorption measurements (BET). Specific surface area, pore volume, and pore size are critical parameters for electrocatalysts.

Figure 3C compares the nitrogen adsorption−desorption isotherms and pore size distribution curves of CB and OLC. Both carbon materials exhibit type IV isotherms with type H3 hysteresis loops, indicating that they are essentially mesoporous materials (i.e., 2−50 nm). The BET surface areas (Table 1) of CB and OLC were determined to be 35.6986 and 375.3579 m^2/g, respectively.

The specific surface area of OLC is more than 10 times higher than that of CB, confirming that OLC comprises much smaller nanoparticles than CB. The Barrett−Joyner−Halenda (BJH) approach was used to assess the pore size distribution of CB and OLC. A continuous pore size distribution within the range of 5−100 nm is observed, which is nearly in direct proportion to the pore diameter increase. The BJH method showed the pore diameter of CB and OLC ranging between 14.8 and 15.8 nm (see insert of Figure 3C), consistent with the mesoporous characteristics. Pore sizes smaller than 4 nm are due to mass loss arising from carbonization, while larger pore sizes (>20 nm) are associated with cavities in the carbon materials. The high specific surface area is important for enhancing the electrocatalytic properties of materials, thus one expects that OLC should provide better catalytic properties than the CB counterpart.

Table 1. Surface Parameters CB and OLC Materials

sample	specific surface area, S_{BET} (m^2/g)	pore volume, V (cm^3/g)	pore size, D (nm)
CB	35.6986	0.1408	15.7771
OLC	375.3579	1.3888	14.7992

Figure 3D shows the comparison of the thermal and derivative gravimetric analyses (TGA and DTGA) of the CB and OLC. It is noted that the onset decomposition temperatures of CB and OLC were 689 and 670 °C, respectively. The first-order derivative peaks are centered at 793 and 756 °C for CB and OLC, respectively. Both CB and OLC are completely burnt with no weight retention, confirming the characteristic properties of carbon.

2.2. Cyclic Voltammetry: Mass Transport and Charge-Transfer Kinetics. Since this work has not been studied by anyone before, this work first sought to understand the cyclic voltammetric (CV) properties of two carbon-based electrodes in a solution of a redox probe. Figure 4A,B compares the CV evolutions of the bare GCE and the GCE modified with CB and OLC at 10 and 150 mV/s, respectively. Table 2 summarizes the CV parameters of the electrodes at the smallest (10 mV/s) and highest (150 mV/s) scan rates. The CV evolutions at different scan rates for the GCE-OLC (Figure 4C) and the GCE-CB (Figure 4E) and their respective plots of peak current against the square root of the scan rates (Figure 4D,F) are given.

The current response at an electrode surface is the result of two inexorably intertwined processes: (i) the mass transport (i.e., the rate at which the analyte diffuses from the bulk electrolyte to the electrode surface) and (ii) charge-transfer kinetics (i.e., transport of electrons or ions across the electrode−electrolyte interface). The CV data reveal important electrochemical information with respect to mass transport and kinetics. First, the plot of peak current (for both anodic (I_{pa}, mA) and cathodic (I_{pc}, mA)) vs the square root of scan rate ($\upsilon^{1/2}$, $(mV/s)^{1/2}$) shows linear curves ($R^2 > 0.99$), which clearly confirms that the electrochemistry at these electrode platforms is a diffusion-controlled process in accordance with the conventional Randles−Sevcik theory. Note that the slopes of the GCE-OLC are about twice that of the GCE-CB, meaning that diffusion is faster at the former than at the latter.

At this juncture, it may be necessary to remind us that the current response from the surface of any porous electrode material (such as OLC) is (i) a dual diffusion process, i.e., semi-infinite planar diffusion (of the analyte molecules toward the macroelectrode surface) and (ii) thin-layer diffusion (i.e., a small volume of analyte solution trapped in pockets within the porous structure).[48,49] Considering that both the thin layer and adsorption effects also show a linear dependence of $\log I_p$ vs

https://doi.org/10.1021/acsomega.2c05722
ACS Omega 2022, 7, 47892−47905

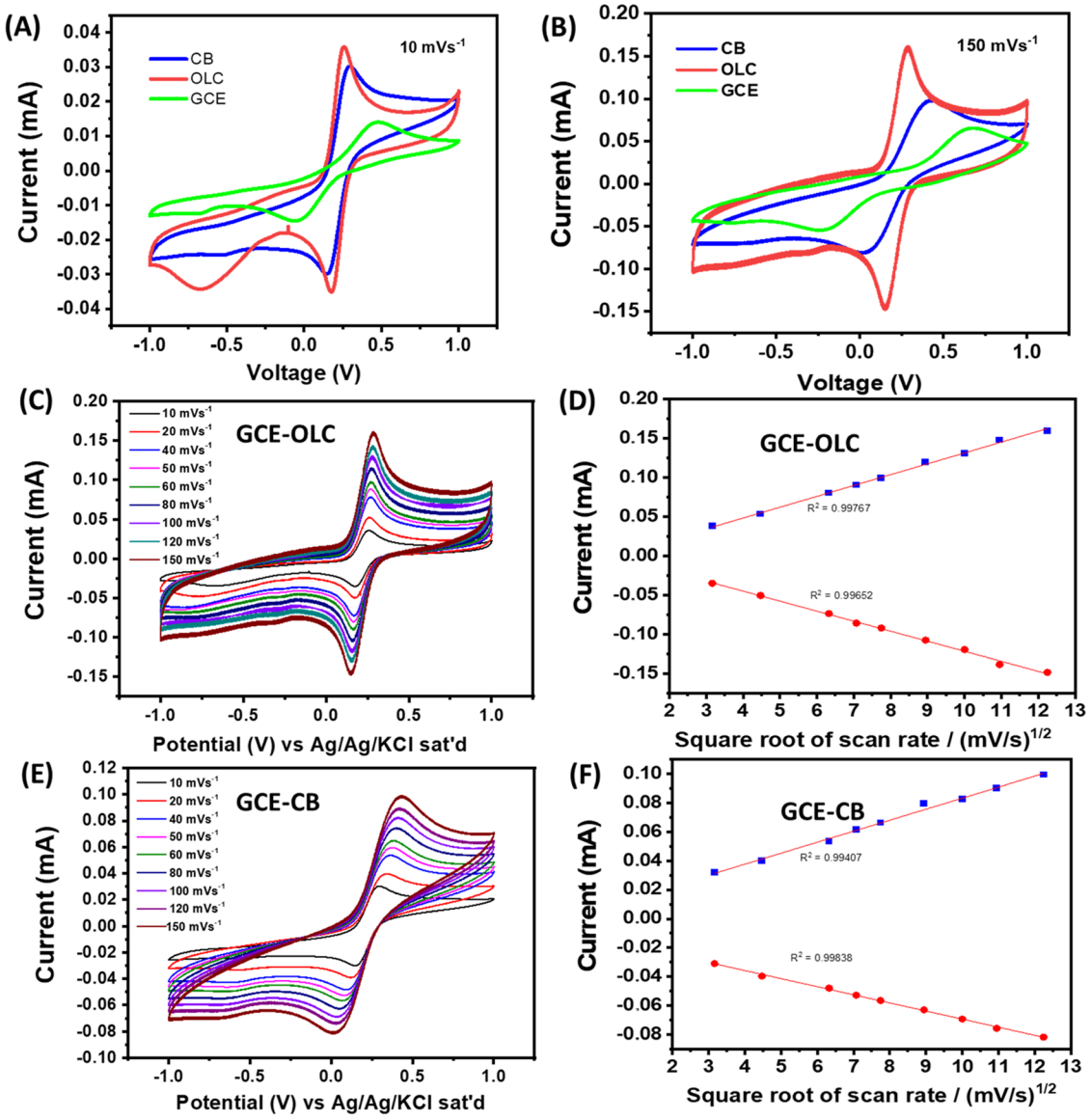

Figure 4. Cyclic voltammograms of the electrode at (A) 10 mV/s and (B) 150 mV/s. CV at different scan rates (10−150 mV/s) for (C) OLC and (E) CB and their corresponding plots of peak currents vs square root of scan rate (D, F), respectively. All data were collected in a redox probe ($[Fe(CN)_6]^{4-}/[Fe(CN)_6]^{3-}$ in 0.1 M KCl).

Table 2. CV Parameters of the OLC- and CB-Based Electrodes Obtained in a Solution of Redox Probe

	bare GCE		GCE/OLC		GCE/CB	
CV parameter	@10 mV/s	@150 mV/s	@10 mV/s	@150 mV/s	@10 mV/s	@150 mV/s
E_{pa}, V	0.460	0.674	0.260	0.292	0.301	0.437
E_{pc}, V	−0.063	−0.251	0.185	0.150	0.157	0.023
ΔE_p, V	0.523	0.925	0.075	0.142	0.144	0.414
$E_{1/2}$, V	0.262	0.463	0.223	0.221	0.229	0.230
I_{pa}, mA	0.014	0.065	0.036	0.159	0.030	0.099
I_{pc}, mA	−0.015	−0.055	−0.035	−0.145	−0.030	−0.082
I_{pa}/I_{pc}	0.933	1.818	1.029	1.097	1.000	1.207

$\log \nu$, it becomes somewhat difficult to distinguish between diffusion and adsorption phenomena, especially if the adsorption is rapidly reversible.[48] However, the value of the slope (b) of the $\log I_p$ vs $\log \nu$ plot provides some insights: when b = 0.5 (pure diffusion process), when b = 1.0 (pure adsorption process), and when b > 0.5 but less than 1.0, it depicts a mixture of diffusion and adsorption processes. In this work, the plot of $\log I_p$ vs $\log \nu$ (for both anodic and cathodic) shows linear curves (R^2 > 0.99 and with slope ∼0.55 for the GCE-OLC and ∼0.4 for the GCE-CB) (figure not shown). These results show that the electrochemistry of the GCE-OLC is mostly diffusion controlled while the GCE-CB shows some resistive behavior. Also, considering the high porosity of the OLC, thin-layer diffusion cannot be ruled out. The inability to

https://doi.org/10.1021/acsomega.2c05722
ACS Omega 2022, 7, 47892−47905

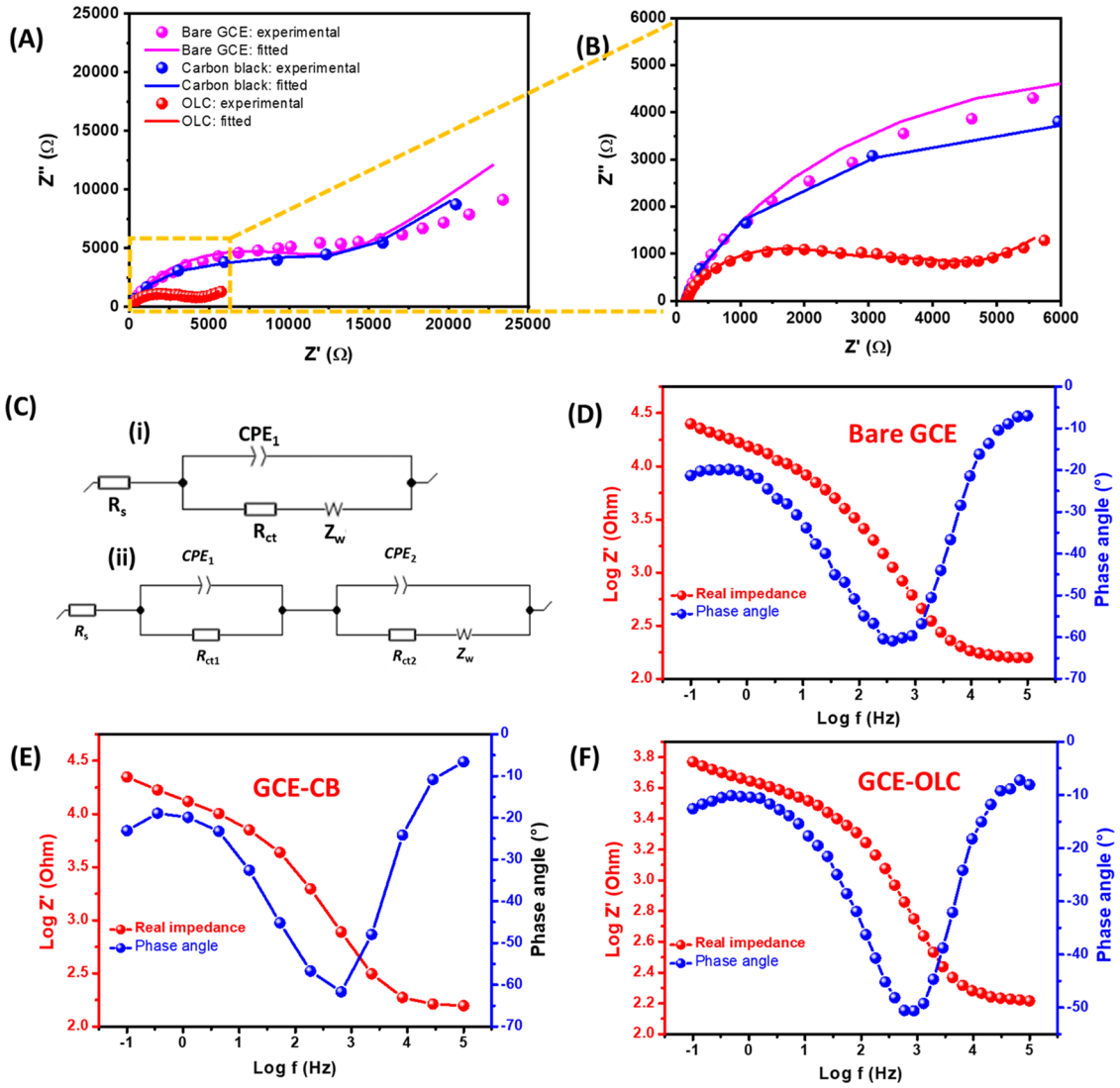

Figure 5. (A) Nyquist plots and (B) zoomed-in image of (A) bare GCE, GCE-CB, and GCE-OLC. (C) Electrical equivalent circuits used to model bare GCE (i) and GCE modified with OLC and CB (ii). (D–F) Bode plots of GCE, GCE-CB, and GCE-OLC, respectively. Data points are experimental, while lines are fitted data using the electrical equivalent circuits. All data were collected in the redox probe ($[Fe(CN)_6]^{4-}$/$[Fe(CN)_6]^{3-}$) in a 0.1 M KCl solution.

observe the adsorptive behavior may be related to the weak or rapidity of adsorption of tramadol on the OLC surface (see discussion on DFT studies) compared to that on the CB.

Second, the ratio of the anodic-to-cathodic peak current (I_{pa}/I_{pc}) gives an insight into the electrochemical kinetics of the electrodes; if the ratio is unity, then the electrode is described as perfectly reversible. The two electrodes showed perfect reversibility ($I_{pa}/I_{pc} \approx 1$).

Third, the value of the peak-to-peak separation potential (ΔE_p, V) describes the extent of the electron-transfer kinetics; the smaller the ΔE_p value, the faster the rate of the electron transfer and vice versa. From the CV data (Table 1), the GCE-OLC exhibits much faster electron-transfer kinetics at small and high scan rates ($\Delta E_p \approx 75$ and 142 mV at 10 and 150 mV/s, respectively) compared to the GCE-CB counterpart ($\Delta E_p \approx$ 144 and 414 mV at 10 and 150 mV/s, respectively). Fourth, the GCE-OLC showed a higher current response (mass transport) than the GCE-CB counterpart. For example, at 150 mV/s, the current response at the GCE-OLC was 0.159 mA compared to 0.099 mA for the GCE-CB. The result is attributed to the high specific surface area and high porous volume of the OLC compared to the CB, which corroborates the BET data.

Finally, the CV curves at different scan rates give further insight into the structural stability of the modified electrodes. It is observed that as the scan rate increase from 10 to 150 mV/s, both the anodic and cathodic peaks potentials of the GCE-CB shift to the right by 136 mV (i.e., from 0.301 to 0.437 V) and left by 134 mV (i.e., from 0.157 to 0.023 V). On the other hand, the GCE-OLC only showed a very small shift (~32 mV) on the anodic peak potential (i.e., from 0.260 to 0.292 V) and ~35 mV shift on the cathodic side (i.e., from 0.185 to 0.150 V). This result clearly showed that the GCE-OLC is the best structural and faster charge transport than the GCE-CB. In other words, the CB electrode exhibits sluggish electron-transfer kinetics.

2.3. Electrochemical Impedance Spectroscopy: Charge-Transfer Kinetics. EIS is very important in understanding the redox properties of an electrocatalyst, which explains its wide application in various areas of electro-

https://doi.org/10.1021/acsomega.2c05722
ACS Omega 2022, 7, 47892−47905

chemistry. Figure 5 compares the EIS data obtained in the redox probe using two carbon-based electrodes.

The electrodes were satisfactorily modeled with a coupled RC-Randles circuit (i.e., with ion-diffusion/Warburg region). The modeled parameters comprise the electrolyte resistance (R_s), the interfacial resistance (R_{int}) arising from the IR drop, the corresponding nonideal capacitance of the interfacial layer or constant-phase element (CPE_1), the charge-transfer resistance (R_{ct}), and its corresponding constant-phase element (CPE_2) due to surface heterogeneity or irregularities of the electrode surface and the Warburg diffusion impedance (Z_W) due to resistance to the ion-diffusion process.

The impedance of the CPE (ZCPE) is defined as eq 1[44,50−54]

$$Z_{CPE} = \frac{1}{Q(jw)^n} \quad (1)$$

where Q is a constant associated with the electrode/electrolyte interface, $j = \sqrt{-1}$, ω is the radial frequency, and the exponent n represents the slope of the plot of $\log Z$ against $\log F$ (i.e., Bode plot). The values of n range between −1 and +1 (i.e., $-1 \leq n \leq 1$: when a = 0, the CPE is a perfect resistor; when $n = 1$, the CPE is a pure capacitor; when $n = -1$, the CPE is an inductor; and when $n = 0.5$, the CPE is equivalent to the Warburg impedance (Z_W)). From Table 3, the total series resistance ($R_s + R_{int} + R_{ct}$) decreases as follows: GCE (15.076 kΩ) > GCE-CB (12.924 kΩ) > GCE-OLC (4.696 kΩ), meaning the electron transfer at the OLC-based electrode is more than 4 times faster than at the CB and GCE. This result corroborates the CV data (see Table 2 for the values of the ΔE_p). The appearance of the CPE in the modeling indicates that the electrode surface is rough and porous. The "n" values (n_1 and n_2) of the CPE range between 0.77 and 0.88, implying that these electrocatalyst materials exhibit a mixed mechanism of pseudocapacitance. Finally, the Z_W value increased as follows: GCE-OLC ≫ GCE-CB > GCE, which indicates that the GCE-OLC allows for faster ionic diffusion than the GCE-CB, which perfectly agrees with the CV data of peak current vs square root of the scan rate.

Table 3. EIS Parameters for the GCE, GCE-CB, and GCE-OLC

EIS parameter	bare GCE	GCE-CB	GCE-OLC
R_s, Ω	145.40 ± 0.32	152.50 ± 0.21	158.5 ± 0.36
CPE_1, $\mu F \cdot s^{(n-1)}$	2.06 ± 0.02	1.321 ± 0.026	1.842 ± 0.038
n_1	0.79	0.87	0.83
R_{int}, Ω		4394 ± 76	2363 ± 35
CPE_2, $\mu F \cdot s^{(n-1)}$		6.286 ± 0.038	38.83 ± 0.01
n_2		0.81	0.77
R_{ct}, Ω	11 732 ± 1.83	8377 ± 106	2174 ± 29
i_0, A	2.2×10^{-7}	3.1×10^{-6}	1.2×10^{-5}
k_{het}, cm/s	3.2×10^{-11}	4.49×10^{-10}	$1{,}73 \times 10^{-9}$
Z_W, Ω $s^{-0.5}$	9358 ± 1	6803 ± 6	952 ± 2

EIS data throws more light on the reversibility of the redox processes by calculating the exchange current (i_0) and the rate constant of the heterogeneous electron transfer (k_{het}) using eqs 2 and 3[55−57]

$$i_0 = \frac{RT}{nFR_{ct}} \quad (2)$$

$$k_{het} = \frac{i_0}{nFA} \quad (3)$$

where A is the geometric surface area of the electrode, R is the gas constant (8.314 J K^{-1} mol^{-1}), T is the Kelvin temperature (273 K), n is the number of electrons transferred, and F is the Faraday constant (96 485.33 C/mol). The higher the values of i_0 and k_{het}, the better the electrocatalysis. Both i_0 and k_{het} decrease as follows: GCE-OLC > GCE-CB > GCE, which clearly corroborates that the electron transport of the GCE-OLC is about a magnitude faster than that of the GCE-CB, with the bare GCE exhibiting a sluggish electron transport.

2.4. Electrocatalytic Detection of Tramadol. Figure 6A compares the CV evolution of the three electrodes in the PBS (pH 7.4) containing 0.5 mM of TR, showing that the peak current responses decrease in the order GCE-OLC (0.157 mA) > GCE-CB (0.028 mA) > GCE (∼0.0). This result means that the GCE-OLC depicts an exceptional current response compared to the GCE-CB counterpart. Figure 6B then compares the current responses of the GCE-OLC in the absence and presence of TR, which clearly proves that the response observed in Figure 6A is indeed due to the oxidation of TR. Important electrocatalytic information can be obtained from CV at different scan rates. Figure 6C shows the effect of different scan rates (10−150 mV/s) on the current response at a given TR concentration (0.5 mM). Following the equation for a totally irreversible anodic diffusion-controlled process (eq 4), a plot of peak current vs square root of scan rate is obtained (Figure 6D).

The excellent linearity of the plot (correlation coefficient, $R^2 = 0.9951$) (eq 4) is indicative of diffusion-controlled process.

$$I_p, \text{A} = 0.0667 \log(\upsilon^{1/2}, \text{ V/s}) - 0.0030, \quad R^2 = 0.9951 \quad (4)$$

From the CV evolutions (Figure 6C), the logarithmic plot of the oxidation peak current vs scan rate (see eq 5) is linear, with a slope of ∼0.63 indicating mixed diffusion- and adsorption-controlled processes. Also, the peak potential (E_p, V) shifts slightly in the positive direction as the scan rate increases. The plot of E_p, V against the $\log \upsilon$ (for scan rates of 50−150 mV/s) showed a linear behavior according to eq 6

$$\log(I_p, \text{A}) = 0.628 \log(\upsilon, \text{ mV/s}) - 3.00, \quad R^2 = 0.9979 \quad (5)$$

$$E_p, \text{V} = 0.129 \text{ mV} \log(\upsilon, \text{ mV/s}) + 0.585, \quad R^2 = 0.9914 \quad (6)$$

This behavior agrees with the conventional equation for an irreversible anodic process (eqs 7 and 8)[58−61]

$$E_p = \frac{b}{2} \log \upsilon + \text{constant} \quad (7)$$

where

$$b = \frac{2.303RT}{(1-\alpha)n_\alpha F} \quad (8)$$

where $b/2$ equals the slope of the plot (while b = Tafel slope), α is the transfer coefficient, n_α is the number of electrons involved in the rate-determining step (rds) of the electrode process, F is the Faraday constant, R is the gas constant, and T is the absolute temperature. From the Tafel slope (i.e., b = 0.258 mV), $(1-\alpha)n_a$ value is ∼0.23. Assuming the one-

https://doi.org/10.1021/acsomega.2c05722
ACS Omega 2022, 7, 47892−47905

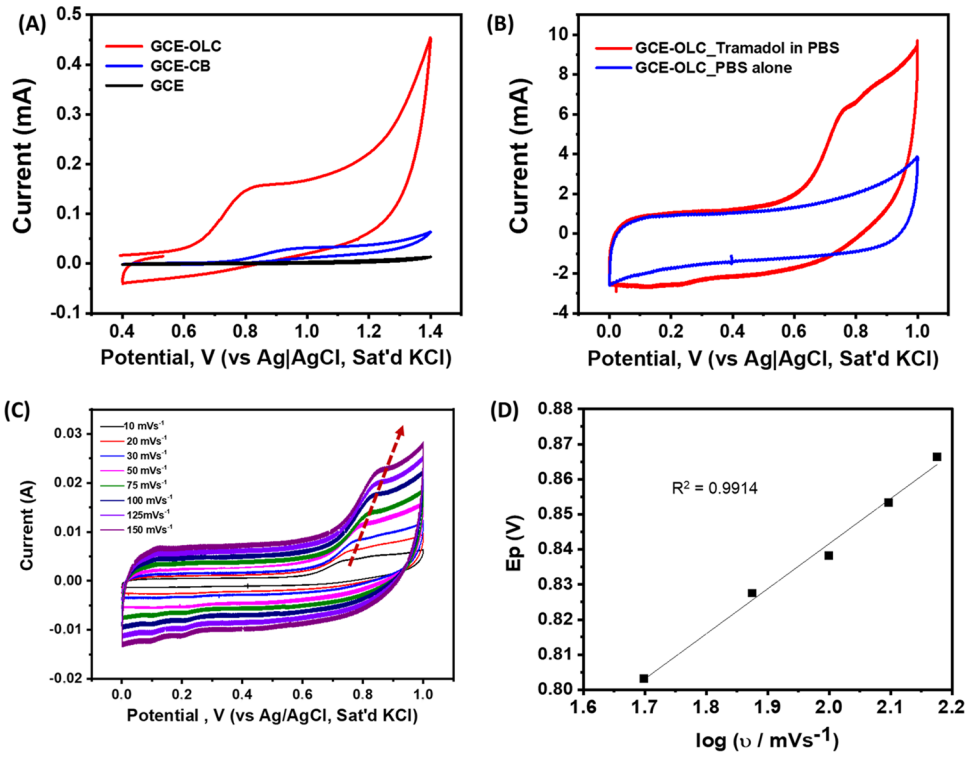

Figure 6. (A) CV evolutions of the GCE, GCE-CB, and GCE-OLC in PBS (pH 7.4) containing 0.5 mM tramadol at 20 mV/s. (B) Comparison of the CVs of GCE-OLC in PBS alone and PBS containing 0.5 mM tramadol at 20 mV/s. (C) CV evolution showing the effect of changing scan rates on the current responses. (D) Plot of peak potential vs log scan rate. All of the data were acquired in PBS containing 0.5 mM tramadol hydrochloride.

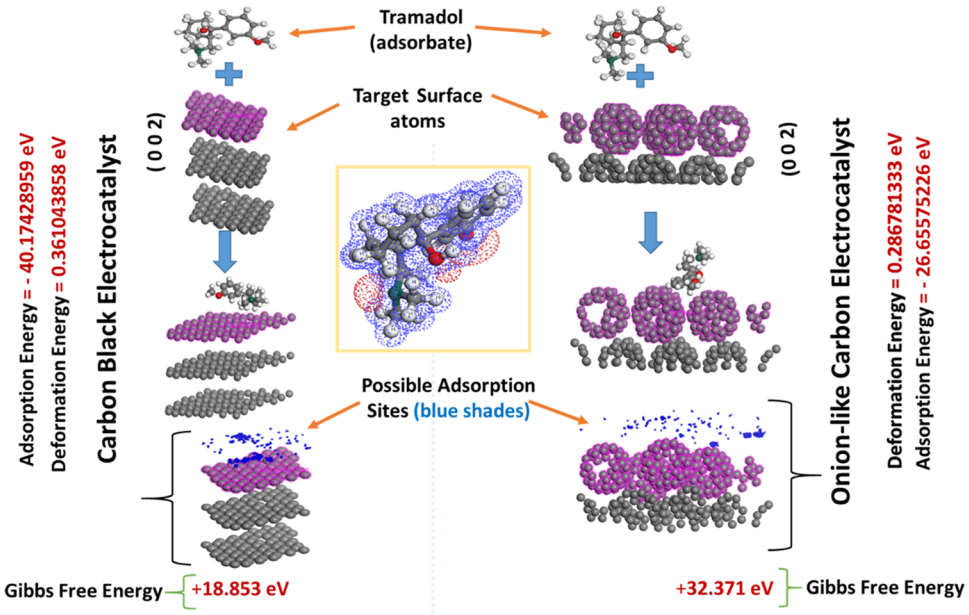

Figure 7. Adsorption sites of tramadol at the surfaces of CB and OLC. The dark blue dots (shades) show that the possible site tramadol molecules are adsorbed. Inset is used to determine the isosurface potentials of tramadol @ ±0.05181 isovalue (au) for tramadol molecule.

electron mechanism in the rds (i.e., n_α = 1), the α of ~0.77 indicates that the activation free energy curve for an irreversible oxidation process for tramadol is asymmetrical.

2.5. Predicting the High Electrocatalytic Activity of OLC over CB toward the Detection of Tramadol: DFT Calculations. The excellent electrocatalytic performance of OLC toward the detection of TR raises an important question of "why is OLC better than CB?" To answer this critical question, we adopted the use of DFT to assist in predicting the interaction of TR with OLC vs CB. This is an important development, as many researchers have used different carbons to detect TR, but, to the best of our knowledge, there is no report o the reason why some carbons are better than others. Thus, this work attempts to fill this knowledge gap.

https://doi.org/10.1021/acsomega.2c05722
ACS Omega 2022, 7, 47892−47905

Table 4. Predicted Energy Values from the DFT Calculations Accompanying the Interaction of Tramadol with the Surfaces of OLC and CB[a]

catalyst	adsorbate	ΔG (eV)	E_{ad} (eV)	E_{def} (eV)	E_F (eV)	E_g (eV)	K.E. (Ha)
CB	n/a	n/a	n/a	n/a	−6.838	0.008	−273.973
	tramadol	18.853	−40.174	0.361	−6.838	0.002	−305.322
OLC	n/a	n/a	n/a	n/a	−6.842	0.123	−124.389
	tramadol	32.371	−26.656	0.2868	−6.831	0.121	−155.815

[a]ΔG = Gibbs free energy; E_{ad}= adsorption energy; E_{def} = deformation energy; E_F = Fermi energy; E_g = energy band gap; K.E. = kinetic energy; n/a = not applicable.

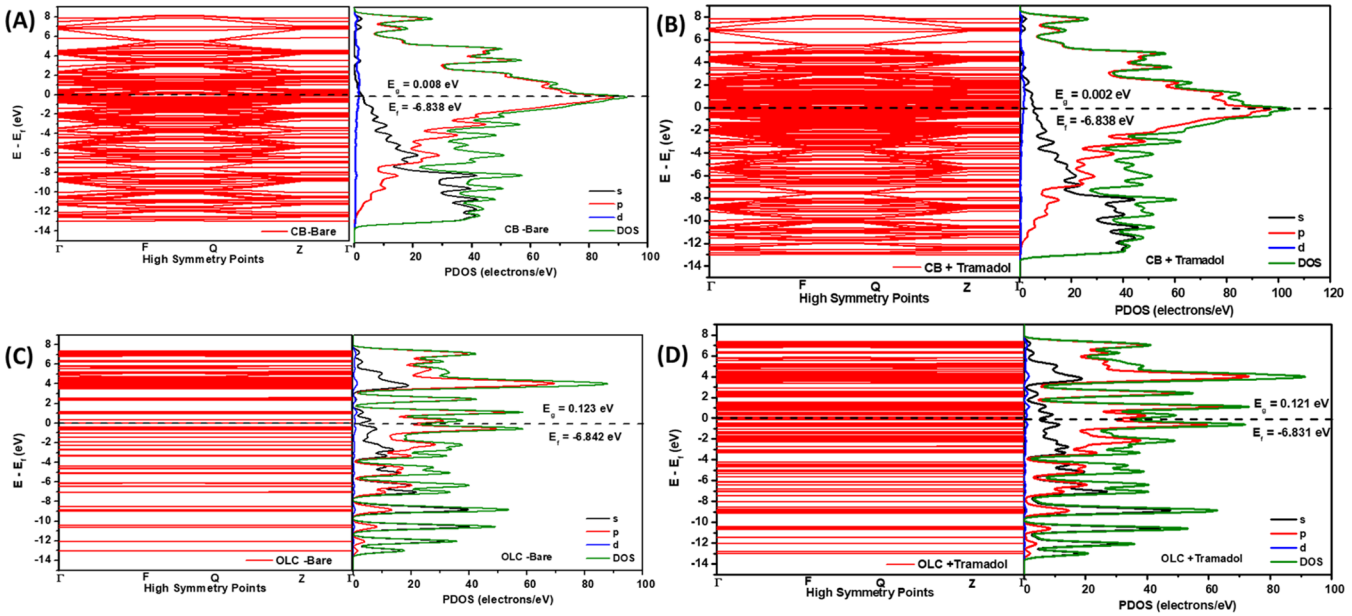

Figure 8. Band structures and PDOS for tramadol adsorbed on (A, B) CB and (C, D) OLC electrodes.

Figure 7 is the schematic representation of the carbon models used to predict the interaction of OLC and CB with the TR molecule. Using the Nanotube Modeler Software, OLC was modeled as fullerene (spherical species), while the CB was modeled as flat molecules (i.e., multiple layers of graphene). From the isosurface potential, oxygen has a higher negative potential (blue shades) compared to nitrogen (red shades), meaning that likely sites of tramadol interaction are dominated by oxygen.

In the DFT calculation, the adsorption energy, E_{ad} (eV), is defined as (eq 9)[43,62,63]

$$E_{ad} = (E_{surface + adsorbate}) - (E_{surface} + E_{adsorbate}) \quad (9)$$

where $E_{surface + adsorbate}$ is the total energy of the interacting catalyst surface and the adsorbate and $E_{surface} + E_{adsorbate}$ is the energies of the bare catalyst surface and the free adsorbate in the gas phase. This equation shows that the more negative the E_{ad} value, the stronger the adsorption. The best-performing electrocatalyst should possess the weakest adsorption strength (E_{ad}, eV) with the TR molecule. According to thermodynamics, the more negative the ΔG value, the weaker the interaction of the adsorbate on the surface of the catalyst. The DFT results (summarized in Table 4) show that E_{ad} and ΔG give the least negative values for the OLC−tramadol complex. Weak adsorption of adsorbate is most preferred in electrocatalysis, thus the weaker adsorption of TR onto OLC compared to CB predicts better electrocatalysis on OLC than on CB.

It is well-known that graphene (single layer of graphite) is far more conducting than fullerene and even carbon nanotubes. Thus, the smaller energy band gap (high conductivity) of the conductive CB (0.008 and 0.002 eV) than that of the OLC (0.123 and 0.121 eV) should be expected. The flat CB makes it easy for it to deform than the curved OLC, thus an easy misalignment of p-orbitals of carbon atoms, meaning that the carbon atoms on the outside walls of the CB exhibit more sp^3 nature than those on the OLC (this is evident in the PDOS and Raman). Considering that the pi−pi interaction between the carbon atoms of TR and the adjacent carbon atoms of the OLC strengthens the deformation of the OLC, it simply means that a more stable deformation does not promote the overlap between the different pi-wave functions, thus weakening the adsorption of TR molecule onto OLC.

DFT predicts that CB exhibits properties inimical for electrocatalysis; a more metallic character (low Eg) and slower kinetics with tramadol than OLC.

To understand the electronic properties of TR on the carbon materials, before and after the adsorption process, DFT calculations on the electronic band structures and the projected density of states (PDOS) were carried out (Figure 8). Prior to the adsorption of the TR molecule onto each of the carbon materials, both the band structure and PDOS show a lower number of states than when TR is adsorbed onto the carbon catalyst. In other words, more electrons are available on the CB−tramadol and OLC−tramadol complexes than on the bare CB or OLC. Unlike the OLC, which shows a change in

https://doi.org/10.1021/acsomega.2c05722
ACS Omega 2022, 7, 47892−47905

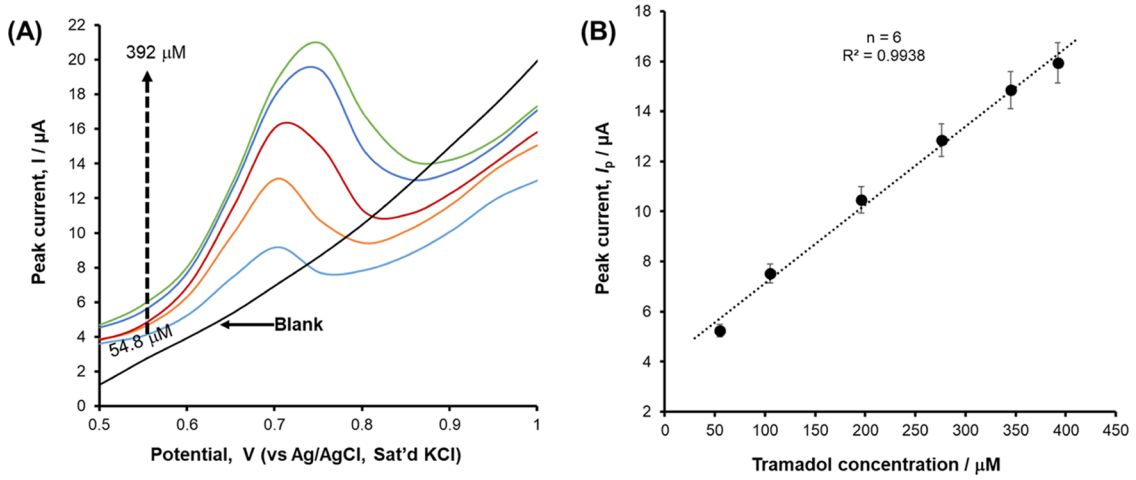

Figure 9. (A) Typical square wave voltammograms obtained in PBS (pH 7.4) containing different concentrations of tramadol (0−392 μM) and (B) plot of peak current response vs concentration of tramadol.

the Fermi energy value upon interaction with TR, the CB did not show any change. Note that upon the interaction of the TR molecule with the OLC catalyst, there is a mismatch in Fermi levels (E_F), which leads to the charge-transfer process. This charge-transfer process leads to a redistribution of partial charge, which enhances the reactivity of the OLC over its CB counterpart.

2.6. Analytical Application of OLC-Based Electrochemical Sensors. *2.6.1. Determination of Raw Tramadol in PBS (pH 7.40).* Figure 9 shows typical concentration studies with SWV using both the GCE-OLC (Figure 9A) and its corresponding linear calibration curve (Figure 9B). The near-vertical curve of the blank suggests some resistivity in the electrolyte under the experimental conditions, but this was somewhat suppressed in the presence of the tramadol drug. Expectedly, this explains one of the reasons why the linear curves could not start from a zero origin. Six replicate measurements were run for each concentration. The anodic peak from the oxidation of tramadol appeared around 0.7 V vs AglAgCl (3 M KCl). The linear equation is as shown below (eq 10)

$$I_{pa},\ \mu A = 0.0315 \pm 0.0003\ [\text{tramadol},\ \mu M] + 3.9940 \pm 0.040 \quad (R^2 = 0.9938) \tag{10}$$

The electrode shows a wide linear range (54.8−392 μM), high sensitivity (m = 0.0313 A/M), and low limit of detection and quantification (LoD ∼ 3.80 μM), determined from LoD = 3 s/m and LoQ = 10 s/m ∼ 12.7 μM, where s is the standard deviation of the intercept (in μA) and m is the slope/sensitivity of the calibration plot (in μA/μM). The values were calculated as the average of six electrodes and are summarized in Table 5.

2.6.2. Determination of Tramadol in Pharmaceutical Sample and Human Serum. To validate that the OLC can be used for the determination of TR using "a point-of-care" type of electrode, a commercial screen-printed carbon electrode (SPCE, Dropsens) was modified with OLC ink and used to determine TR in two different real sample solutions, i.e., "tramadol hydrochloride" capsule (50 mg tramadol) in (i) PBS (pH 7.40) (Figure 10A,B) and (ii) artificial human blood/serum diluted in PBS (pH 7.40) (Figure 10C,D). Human serum solution was first prepared by dissolving it in PBS (pH 7.40) at a 1:100 v/v ratio and then tramadol was dissolved. In

Table 5. Summary of Results Obtained in This Work for Electrochemical Sensing of Tramadol, Using the DPV Method

sample	technique	electrolyte	LCR, μM	LoD, μM	LoQ, μM
GCE-OLC	DPV	PBS (pH 7.4)	54.8−392	3.80	12.70
SPE-OLC	DPV	PBS (pH 7.4)	27.9−345	17.5	58.14
SPE-OLC	DPV	drug, PBS (pH 7.4)	10.6−253	2.34	7.81
SPE-OLC	DPV	serum, PBS (pH 7.4)	10.6−253	4.70	15.90

all cases, the OLC-modified SPCE successfully detected TR, with the anodic peak current appearing at around 0.70 V vs Agl AgCl (sat'd KCl) as was also seen for the pure tramadol samples in the GCE-OLC electrode. Each of the four capsules was carefully opened, and the contents were accurately weighed to be ca. 82 mg (meaning that the weight of excipients is ca. 39% per capsule which, according to the description on the label comprises colloidal silicon dioxide, magnesium stearate, microcrystalline cellulose, and sodium starch glycolate). A stock solution of each powder (3.75 mg in 10 mL, i.e., ∼2.29 mg "pure" tramadol chloride in 10 mL or 0.87 M tramadol chloride) was prepared in PBS (pH 7.40) as well as in human serum solution. Considering the importance of determining TR in the presence of real interfering materials in complex matrices such as human serum and excipient-rich tramadol capsule sample, no further treatment of the solution (such as filtering to obtain "pure" supernatant) was carried out.

A standard addition method was used to carry out the DPV analysis at different concentrations (in the range of 20 nm to 0.45 μM) as shown in Figure 10. As should be expected, both DPV curves show broad peaks (Figure 10A,C) compared to the pure tramadol (shown in Figure 9A) due to the presence of several interfering species in the capsule and human serum. As should be expected, the resistivity introduced by these interferents and a blank electrolyte would lead to the linear calibration curves not starting from the origin, despite efforts to subtract the background current. However, interestingly, the tramadol peak was still around 0.7 V (vs AglAgCl Sat'd KCl) as in pure tramadol analysis.

The equations for the resulting calibration plots were as follows (eqs 11 and 12)tramadol capsule (pH 7.4):

https://doi.org/10.1021/acsomega.2c05722
ACS Omega 2022, 7, 47892−47905

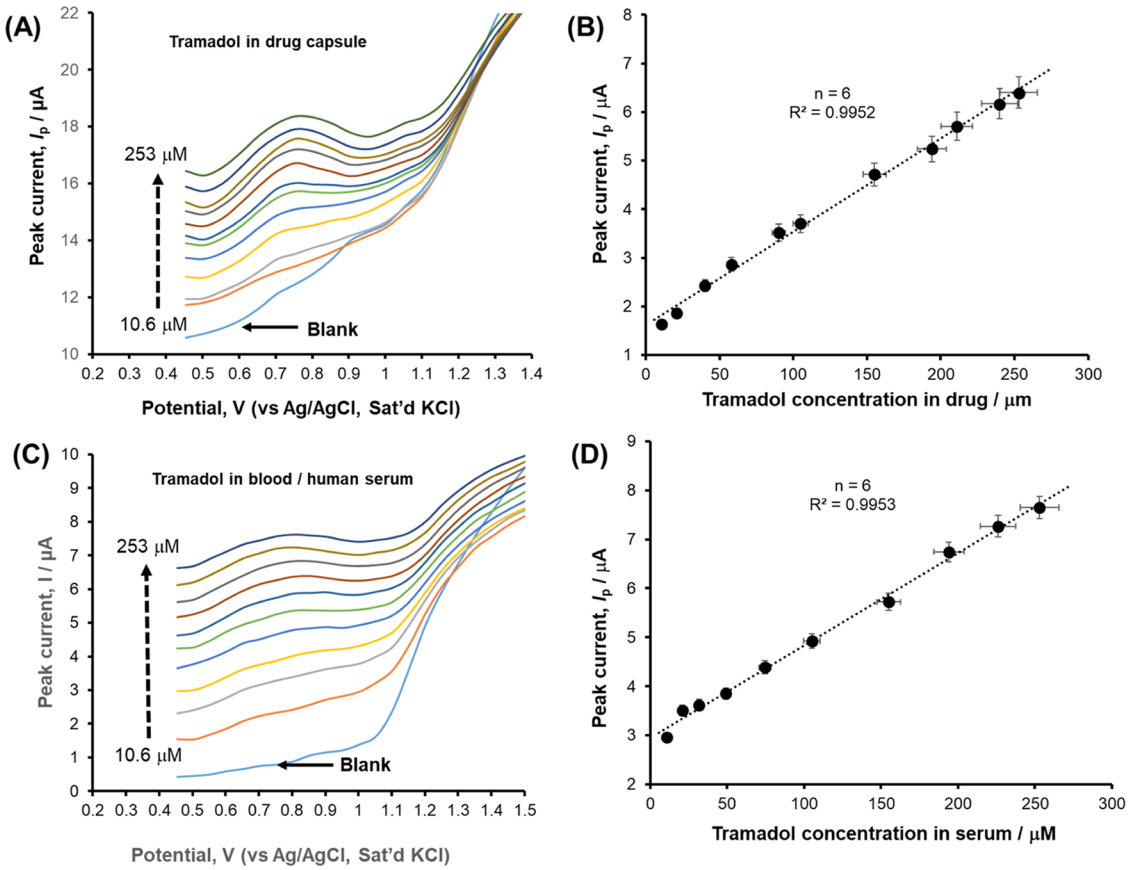

Figure 10. Typical SWV curves (A, C) obtained in real sample analysis using a screen-printed carbon electrode (SPCE) modified with OLC (SPCE-OLC) for tramadol in drug capsule (A) and in human serum solution (C). The plot of background-subtracted peak current responses vs the concentrations of tramadol (B, D).

$$I_{pa},\ \mu A = 0.0192 \pm 0.0002\ [\text{tramadol},\ \mu M] + 1.6154 \pm 0.015 \quad (R^2 = 0.9955) \tag{11}$$

tramadol in human serum (pH 7.4):

$$I_{pa},\ \mu A = 0.0188 \pm 0.0002\ [\text{tramadol},\ \mu M] + 2.9518 \pm 0.0300 \quad (R^2 = 0.9953) \tag{12}$$

The contents of TR hydrochloride in each capsule were calculated to be 49.78 mg per tablet with an RSD of 3.2% (n = 5), which is close to the labeled amount of 50 mg. The LoD and LoQ for the drug (2.34 and 7.81 μM, respectively) and for the serum (4.70 and 15.9 μM, respectively) were obtained. Although the key focus of this investigation is on the fundamental science and electrochemistry, it is interesting however to see that the results obtained in this work are comparable with many studies, for example, with carbon nanoparticles[33] and a dual-carbon paste electrode modified with phosphotungstic acid and silicomolybdic acid.[32] Importantly, although this work has not been optimized to improve detection limits, it should be noted that these observed detection limits are quite satisfactory, especially if one considers that the toxic effects of TR only occur when the blood tramadol concentration is greater than 1 mg/L (i.e., 3.8 μM)[4,64] and, in most cases, when the blood tramadol concentrations are within the range of 1.6−61.8 mg/L (i.e., 6.07−234.64 μM),[65−68] which are several times greater than the normal therapeutic range of 0.1−0.3 mg/L (i.e., 0.38−1.14 μM).[64] Indeed, the results show the potential for the use of OLC as an electrocatalytic platform for the sensitive detection of tramadol.

3. CONCLUSIONS

This work describes the first report on the use of OLC (vs conductive carbon black) as an electrode platform for the detection of tramadol, an important drug of abuse. OLC-modified glassy carbon electrode (GCE-OLC) shows a wide linear concentration range for tramadol (ca. 55−392 μM) with high sensitivity and low limit of detection and quantification. OLC-modified screen-printed electrode (SPE-OLC) was successfully deployed in the determination of tramadol in human serum samples and pharmaceutical formulation. The OLC-based electrochemical sensor promises to be useful for the sensitive and accurate detection of tramadol in clinics, quality control, and routine quantification of tramadol drugs in pharmaceutical formulations. Theoretical calculations (DFT) predicted that OLC (and possibly spherically shaped carbons) rather than conductive carbon black (and possibly other flat-shaped carbons such as graphene) are the most likely carbon electrodes for the sensitive electrocatalytic detection of tramadol. This work has opened doors for future research. For example, further work is needed for other models or morphologies of carbons such as nanotubes, diamond-shaped, nanofibers, nanowires, fishbones, etc for the sensitive detection of tramadol and related drugs. Given the high sensitivity of the OLC, future research on modification with low-cost transition-metal oxides should be considered.

https://doi.org/10.1021/acsomega.2c05722
ACS Omega 2022, 7, 47892−47905

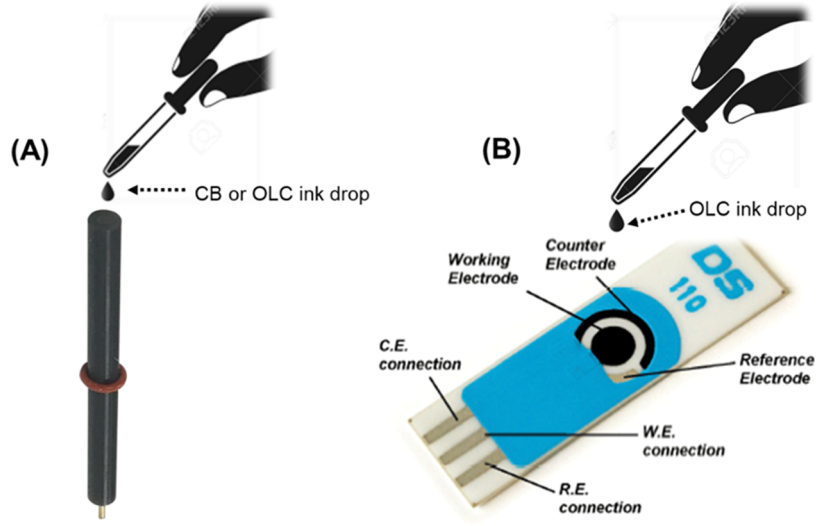

Figure 11. Electrode modification for tramadol electrocatalytic oxidation and sensing. The images are modified by K.I.O. from the photographs obtained from electrode suppliers: (A) courtesy of BASi, copyright 2022, and (B) courtesy of Metrohm Dropsens, copyright 2022.

4. METHODS

4.1. Materials, Reagents, and Methods. Conductive carbon black (TIMICAL SUPER C45, 45 m^2/g) was obtained from Gelon, China, while OLC was synthesized from high-purity (98−99%) nanodiamond powder (NaBond Technologies) by annealing in a muffle furnace at 1300 °C for 3 h in an argon atmosphere. All other reagents were of analytical grade and purchased from Sigma-Aldrich without further purification. Human serum (product number H6914) was obtained from Sigma-Aldrich/Merck, while tramadol pharmaceutical formulation (Austell Tramadol capsule 50 mg, tramadol HCl 50 mg, AUSTELL South Africa; Batch No.: MG 20567; Exp: 08/2023) was donated by a local pharmacy store.

4.2. Physical Property Characterization. Both OLC and CB were characterized using powder X-ray diffraction (PXRD) (Bruker D2 Phaser X-ray diffractometer equipped with a monochromatic Cu Kα X-rays at λ = 1.5406 Å) to investigate the extent of crystallinity. Scanning electron microscopy (SEM) measurements were conducted to establish the morphological properties. The specific surface areas of the samples were obtained with the Brunauer−Emmett−Teller (BET) method using the Micromeritics TriStar II 3000 area and a porosity analyzer instrument. Raman spectroscopy (Bruker Senterra laser Raman spectrometer) was used to verify the extent of graphitization of the carbon bond vibration. Thermal properties were investigated with the Perkin Elmer thermogravimetric analyzer (TGA)/differential thermogravimetric analysis (DTGA) 6000. In a standard run, 10 mg of the samples was placed in a high-temperature alumina sample cup that was supported on an analytical balance located in the furnace chamber of the analyzer and the sample was heated in the air (5 °C/min) from 35 to 900 °C. Initially, the instrument uses nitrogen gas for purging (20 mL/min) while holding at 35 °C for 5 min.

4.3. Electrochemical Detection Procedure. Electrochemical measurements were conducted with an SP300 Bio-Logic potentiostat (running on EC-Lab software). A three-electrode configuration was used: a glassy carbon electrode (GCE, diameter 3.0 mm, 0.071 cm^2) modified with either OLC or CB ink as the working electrode, a platinum wire as the counter electrode, and an AglAgCl electrode (3 M KCl) as the reference electrode. Ultrapure water with a resistivity of 18.2 MΩ cm was obtained from a Milli-Q water system (Millipore Corp., Bedford, MA) and used throughout the preparation of solutions. Analytical grade KH_2PO_4 and K_2HPO_4 were used for the preparation of the phosphate buffer solutions (PBS, pH 7.4). The GCE was cleaned by proper polishing on a pad using alumina (Al_2O_3; nanopowder Aldrich) slurry, followed by ultrasonic stirring in ethanol and acetone. The carbon ink was prepared by dispersing the powder (1 mg) in ethanol (1 mL) and adding 100 μL of Nafion (5 wt %) to increase the adhesion of the catalyst material on the GCE. The mixture was sonicated for 30 min to obtain a homogeneous mixture. The catalyst ink (10 μL) was then deposited on the GCE in a dropwise fashion and allowed to dry (Figure 11). Electrochemical impedance spectroscopy (EIS) experiments were carried out in the frequency range of 100 kHz and 10 MHz at an amplitude of 10 mV. Redox probe (3 mM $K_4Fe(CN)_6/K_3Fe(CN)_6$ (1:1 mol ratio) dissolved in 0.1 M KCl) was used to determine the charge-transfer kinetics of the GCE-immobilized carbon catalysts. The EIS was performed at an equilibrium potential ($E_{1/2}$) of the redox probe (0.15 V vs AglAgCl, 3 M KCl) as observed from prior cyclic voltammetry experiments. For real sample analysis (i.e., commercial tramadol capsules and in human serum), only OLC-modified screen-printed carbon electrodes (SPCE, DropSens) were used. The DPV parameters were 50 mV (pulse amplitude), 0.05 s (pulse width), and 0.2 s (pulse period).

The modified electrodes (of GCE and SPE) were used to conduct the electrocatalysis and detection of TR drug samples (pure raw TR and pharmaceutical formulation). Prior to measurements of the TR, blank electrolyte scans were run several times until a stable background current was achieved. The DPV scans in the PBS buffer solution were measured for several concentrations of the tramadol hydrochloride by successively injecting it into the cell with a micropipette from a stock solution (0.5 nM TR). For the human serum measurements, the serum was diluted as 1:100 in PBS, and TR was injected from the stock solution.

4.4. Density Functional Theory (DFT) Calculations. DFT simulations were performed at the supercomputational

https://doi.org/10.1021/acsomega.2c05722
ACS Omega 2022, 7, 47892−47905

facilities at the Centre for High-Performance Computing (CHPC, Cape Town, South Africa) using the BIOVIA Material Studio Suites and employing an adsorption locator tool module. TR was used as the adsorbate on both CB and OLC models. Supercells of 3 × 3 were modeled for carbon electrocatalysts, followed by geometric relaxation calculations with threshold energy set at 10^{-6} eV for convergence to be achieved. The modeled TR was cleaned using the Material Studio cleaning tool, prior to its adsorption. The minimum adsorption distance was set at 5 Å. DMol^3, another module of the BIOVIA Materials Studio, was used to calculate the electronic properties. The same threshold energy as that used for adsorption was set for the calculations of electronic and energy properties. Condensed-phase Optimization Molecular Potential for Atomistic Simulation Studies (COMPASS), forcefield was used since it guarantees reliable theoretical results.

AUTHOR INFORMATION

Corresponding Author

Kenneth I. Ozoemena − *Molecular Sciences Institute, School of Chemistry, University of the Witwatersrand, Johannesburg 2050, South Africa;* orcid.org/0000-0001-7107-7003; Email: Kenneth.ozoemena@wits.ac.za

Authors

Tobechukwu J. Ehirim − *Molecular Sciences Institute, School of Chemistry, University of the Witwatersrand, Johannesburg 2050, South Africa*

Okoroike C. Ozoemena − *Molecular Sciences Institute, School of Chemistry, University of the Witwatersrand, Johannesburg 2050, South Africa*

Patrick V. Mwonga − *Molecular Sciences Institute, School of Chemistry, University of the Witwatersrand, Johannesburg 2050, South Africa*

Aderemi B. Haruna − *Molecular Sciences Institute, School of Chemistry, University of the Witwatersrand, Johannesburg 2050, South Africa*

Thapelo P. Mofokeng − *Molecular Sciences Institute, School of Chemistry, University of the Witwatersrand, Johannesburg 2050, South Africa*

Karolien De Wael − *A-Sense Lab, Department of Bioscience Engineering and NANOlab Center of Excellence, University of Antwerp, 2020 Antwerp, Belgium;* orcid.org/0000-0003-4495-0748

Complete contact information is available at: https://pubs.acs.org/10.1021/acsomega.2c05722

Notes

The authors declare no competing financial interest.

[‖]O.C.O. was a Wits visiting student during the course of this work.

ACKNOWLEDGMENTS

The authors are grateful to the support of the NRF (South Africa)/FWO (Belgium) Joint Science and Technology Research Collaboration for the project "Electrochemistry and nanostructured electrocatalysts for tackling substance abuse" (UID No. 120463) and DSI-NRF-Wits SARChI Chair in Materials Electrochemistry and Energy Technologies (MEET) (UID No. 132739). T.J.E. thanks the University of the Witwatersrand (Wits) and NRF for supporting his PhD project.

REFERENCES

(1) Gong, L.; Stamer, U. M.; Tzvetkov, M. V.; Altman, R. B.; Klein, T. E. PharmGKB summary: tramadol pathway. *Pharmacogenet. Genomics* **2014**, *24*, 374−380.

(2) Agrawal, S.; Patel, P. R.; Gundloori, R. V. N. Proteins as Nanocarriers To Regulate Parenteral Delivery of Tramadol. *ACS Omega* **2019**, *4*, 6301−6310.

(3) Saccomanni, G.; Del Carlo, S.; Giorgi, M.; Manera, C.; Saba, A.; Macchia, M. Determination of tramadol and metabolites by HPLC-FL and HPLC-MS/MS in urine of dogs. *J. Pharm. Biomed. Anal.* **2010**, *53*, 194−199.

(4) Solarino, B.; Riesselmann, B.; Buschmann, C. T.; Tsokos, M. Multidrug poisoning involving nicotine and tramadol. *Forensic Sci. Int.* **2010**, *194*, e17−e19.

(5) Subedi, M.; Bajaj, S.; Kumar, M. S.; Yc, M. An overview of tramadol and its usage in pain management and future perspective. *Biomed. Pharmacother.* **2019**, *111*, 443−451.

(6) Murashova, U. A.; Skalkina, L. V.; Kazakov, P. V.; Mirzabekova, N. S. Development of Chromatographic Methods for Assay of Contaminants of Russian-Made Tramadol Hydrochloride Substance. *Pharm. Chem. J.* **2020**, *54*, 766−771.

(7) Hassamal, S.; Miotto, K.; Dale, W.; Danovitch, I. Tramadol: understanding the risk of serotonin syndrome and seizures. *Am. J. Med.* **2018**, *131*, 1382.

(8) Chikezie, U. E.; Ebuenyi, I. D. Tramadol misuse in the Niger Delta; A review of cases presenting within a year. *J. Subst. Use* **2019**, *24*, 487−491.

(9) Peprah, P.; Agyemang-Duah, W.; Appiah-Brempong, E.; Akwasi, A. G.; Morgan, A. K. "With tramadol, I ride like a Jaguar": a qualitative study of motivations for non-medical purpose tramadol use among commercial vehicle operators in Kumasi, Ghana. *Subst. Abuse Treat. Prev. Policy* **2020**, *15*, 49.

(10) Cole, J. B.; Sattiraju, S.; Bilden, E. F.; Asinger, R. W.; Bertog, S. C. Isolated tramadol overdose associated with Brugada ECG pattern. *Pacing Clin. Electrophysiol.* **2012**, *35*, e219−e221.

(11) Belin, N.; Clairet, A.-L.; Chocron, S.; Capellier, G.; Piton, G. Refractory cardiogenic shock during tramadol poisoning: a case report. *Cardiovasc. Toxicol.* **2017**, *17*, 219−222.

(12) Zimmermann, S. G.; Schmukat, A.; Schulz, M.; Benner, J.; Gunten, U.; Ternes, T. A. Kinetic and mechanistic investigations of the oxidation of tramadol by ferrate and ozone. *Environ. Sci. Technol.* **2012**, *46*, 876−884.

(13) Amin, S.; Hameed, A.; Memon, N.; Solangi, A. R.; Aslam, M.; Sirajuddin; Soomro, M. T. The efficacy of the Nafion blended CTAB protected Au nanoparticles for the electrochemical detection of tramadol in wastewater: A parametric investigation. *J. Environ. Chem. Eng.* **2016**, *4*, 3825−3834.

(14) Du, P.; Zhou, Z.; Wang, Z.; Xu, Z.; Zheng, Q.; Li, X.; He, J.; Li, X.; Cheng, H.; Thai, P. K. Analysing wastewater to estimate fentanyl and tramadol use in major Chinese cities. *Sci. Total Environ.* **2021**, *795*, No. 148838.

(15) Curticapean, A.; Muntean, D.; Curticapean, M.; Dogaru, M.; Vari, C. Optimized HPLC method for tramadol and O-desmethyl tramadol determination in human plasma. *J. Biochem. Biophys. Methods* **2008**, *70*, 1304−1312.

(16) Vlase, L.; Leucuta, S. E.; Imre, S. Determination of tramadol and O-desmethyltramadol in human plasma by high-performance liquid chromatography with mass spectrometry detection. *Talanta* **2008**, *75*, 1104−1109.

(17) Ding, S. N.; Xu, J. J.; Zhang, W. J.; Chen, H. Y. Tris(2,2'-bipyridyl)ruthenium(II)-Zirconia-Nafion composite modified electrode applied as solid-state electrochemiluminescence detector on electrophoretic microchip for detection of pharmaceuticals of tramadol, lidocaine and ofloxacin. *Talanta* **2006**, *70*, 572−577.

(18) Madrakian, T.; Afkhami, A.; Mahmood-Kashani, H.; Ahmadi, M. Superparamagnetic surface molecularly imprinted nanoparticles for sensitive solid-phase extraction of tramadol from urine samples. *Talanta* **2013**, *105*, 255−261.

https://doi.org/10.1021/acsomega.2c05722
ACS Omega 2022, 7, 47892−47905

(19) Abu-Shawish, H. M.; Ghalwa, N. A.; Zaggout, F. R.; Saadeh, S. M.; Al-Dalou, A. R.; Assi, A. A. A. Improved determination of tramadol hydrochloride in biological fluids and pharmaceutical preparations utilizing a modified carbon paste electrode. *Biochem. Eng. J.* **2010**, *48*, 237−245.
(20) Afkhami, A.; Khoshsafar, H.; Bagheri, H.; Madrakian, T. Preparation of NiFe(2)O(4)/graphene nanocomposite and its application as a modifier for the fabrication of an electrochemical sensor for the simultaneous determination of tramadol and acetaminophen. *Anal. Chim. Acta* **2014**, *831*, 50−59.
(21) Aflatoonian, M. R.; Tajik, S.; Aflatoonian, B.; Beitollahi, H.; Zhang, K.; Le, Q. V.; Cha, J. H.; Jang, H. W.; Shokouhimehr, M.; Peng, W. A Screen-Printed Electrode Modified With Graphene/Co3O4 Nanocomposite for Electrochemical Detection of Tramadol. *Front. Chem.* **2020**, *8*, No. 562308.
(22) Arabali, V.; Malekmohammadi, S.; Karimi, F. Surface amplification of pencil graphite electrode using CuO nanoparticle/polypyrrole nanocomposite; a powerful electrochemical strategy for determination of tramadol. *Microchem. J.* **2020**, *158*, No. 105179.
(23) Atta, N. F.; Ahmed, R. A.; Amin, H. M. A.; Galal, A. Monodispersed Gold Nanoparticles Decorated Carbon Nanotubes as an Enhanced Sensing Platform for Nanomolar Detection of Tramadol. *Electroanalysis* **2012**, *24*, 2135−2146.
(24) Babaei, A.; Taheri, A. R.; Afrasiabi, M. A multi-walled carbon nanotube-modified glassy carbon electrode as a new sensor for the sensitive simultaneous determination of paracetamol and tramadol in pharmaceutical preparations and biological fluids. *J. Braz. Chem. Soc.* **2011**, *22*, 1549−1558.
(25) Jahromi, Z.; Mirzaei, E.; Savardashtaki, A.; Afzali, M.; Afzali, Z. A rapid and selective electrochemical sensor based on electrospun carbon nanofibers for tramadol detection. *Microchem. J.* **2020**, *157*, No. 104942.
(26) Khairy, M.; Banks, C. E. A screen-printed electrochemical sensing platform surface modified with nanostructured ytterbium oxide nanoplates facilitating the electroanalytical sensing of the analgesic drugs acetaminophen and tramadol. *Microchim. Acta* **2020**, *187*, 126.
(27) Madrakian, T.; Alizadeh, S.; Bahram, M.; Afkhami, A. A novel electrochemical sensor based on magneto LDH/Fe3O4 nanoparticles @ glassy carbon electrode for voltammetric determination of tramadol in real samples. *Ionics* **2017**, *23*, 1005−1015.
(28) Mohamed, M. A.; Atty, S. A.; Salama, N. N.; Banks, C. E. Highly Selective Sensing Platform Utilizing Graphene Oxide and Multiwalled Carbon Nanotubes for the Sensitive Determination of Tramadol in the Presence of Co-Formulated Drugs. *Electroanalysis* **2017**, *29*, 1038−1048.
(29) Mohammadi, S.; Taher, M. A.; Beitollahi, H. A hierarchical 3D camellia-like molybdenum tungsten disulfide architectures for the determination of morphine and tramadol. *Microchim. Acta* **2020**, *187*, 312.
(30) Mynttinen, E.; Wester, N.; Lilius, T.; Kalso, E.; Koskinen, J.; Laurila, T. Simultaneous electrochemical detection of tramadol and O-desmethyltramadol with Nafion-coated tetrahedral amorphous carbon electrode. *Electrochim. Acta* **2019**, *295*, 347−353.
(31) Atta, N. F.; Abdo, G. G.; Elzatahry, A.; Galal, A.; Hassan, S. H. Designed electrochemical sensor based on metallocene modified conducting polymer composite for effective determination of tramadol in real samples. *Can. J. Chem.* **2021**, *99*, 437−446.
(32) Abu-Shawish, H. M.; Ghalwa, N. A.; Zaggout, F. R.; Saadeh, S. M.; Al-Dalou, A. R.; Abou Assi, A. A. Improved determination of tramadol hydrochloride in biological fluids and pharmaceutical preparations utilizing a modified carbon paste electrode. *Biochem. Eng. J.* **2010**, *48*, 237−245.
(33) Ghorbani-Bidkorbeh, F.; Shahrokhian, S.; Mohammadi, A.; Dinarvand, R. Simultaneous voltammetric determination of tramadol and acetaminophen using carbon nanoparticles modified glassy carbon electrode. *Electrochim. Acta* **2010**, *55*, 2752−2759.
(34) Keller, N.; Maksimova, N. I.; Roddatis, V. V.; Schur, M.; Mestl, G.; Butenko, Y. V.; Kuznetsov, V. L.; Schlögl, R. The catalytic use of onion-like carbon materials for styrene synthesis by oxidative dehydrogenation of ethylbenzene. *Angew. Chem., Int. Ed.* **2002**, *41*, 1885−1888.
(35) Palaniyandy, N.; Kebede, M. A.; Ozoemena, K. I.; Mathe, M. K. Rapidly microwave-synthesized SnO2 nanorods anchored on onion-Like carbons (OLCs) as anode material for lithium-ion batteries. *Electrocatalysis* **2019**, *10*, 314−322.
(36) Palaniyandy, N.; Kebede, M. A.; Raju, K.; Ozoemena, K. I.; Le Roux, L.; Mathe, M. K.; Jayaprakasam, R. α-MnO2 nanorod/onion-like carbon composite cathode material for aqueous zinc-ion battery. *Mater. Chem. Phys.* **2019**, *230*, 258−266.
(37) Makgopa, K.; Ejikeme, P. M.; Jafta, C. J.; Raju, K.; Zeiger, M.; Presser, V.; Ozoemena, K. I. A high-rate aqueous symmetric pseudocapacitor based on highly graphitized onion-like carbon/birnessite-type manganese oxide nanohybrids. *J. Mater. Chem. A* **2015**, *3*, 3480−3490.
(38) Makgopa, K.; Raju, K.; Ejikeme, P. M.; Ozoemena, K. I. High-performance Mn3O4/onion-like carbon (OLC) nanohybrid pseudocapacitor: Unravelling the intrinsic properties of OLC against other carbon supports. *Carbon* **2017**, *117*, 20−32.
(39) Choudhury, S.; Srimuk, P.; Raju, K.; Tolosa, A.; Fleischmann, S.; Zeiger, M.; Ozoemena, K. I.; Borchardt, L.; Presser, V. Carbon onion/sulfur hybrid cathodes via inverse vulcanization for lithium−sulfur batteries. *Sustainable Energy Fuels* **2018**, *2*, 133−146.
(40) Ozoemena, O. C.; Ehirim, T. J.; Khawula, T.; Makgopa, K.; Shai, L. J.; Ozoemena, K. I. Bovine Serum Albumin-Dependent Charge-Transfer Kinetics Controls the Electrochemical Immunosensitive Detection: Vibrio cholerae as a Model Bioanalyte. *Electrocatalysis* **2021**, *12*, 595−604.
(41) Ozoemena, O. C.; Shai, L. J.; Maphumulo, T.; Ozoemena, K. I. Electrochemical sensing of dopamine using onion-like carbons and their carbon nanofiber composites. *Electrocatalysis* **2019**, *10*, 381−391.
(42) Ejikeme, P. M.; Makgopa, K.; Raju, K.; Ozoemena, K. I. Promotional Effects of Nanodiamond-Derived Onion-Like Carbons on the Electrocatalytic Properties of Pd-MnO2 for the Oxidation of Glycerol in Alkaline Medium. *ChemElectroChem* **2016**, *3*, 2243−2251.
(43) Ogada, J. J.; Ipadeola, A. K.; Mwonga, P. V.; Haruna, A. B.; Nichols, F.; Chen, S.; Miller, H. A.; Pagliaro, M. V.; Vizza, F.; Varcoe, J. R.; et al. CeO2 Modulates the Electronic States of a Palladium Onion-Like Carbon Interface into a Highly Active and Durable Electrocatalyst for Hydrogen Oxidation in Anion-Exchange-Membrane Fuel Cells. *ACS Catal.* **2022**, *12*, 7014−7029.
(44) Mofokeng, T. P.; Tetana, Z. N.; Ozoemena, K. I. Defective 3D nitrogen-doped carbon nanotube-carbon fibre networks for high-performance supercapacitor: Transformative role of nitrogen-doping from surface-confined to diffusive kinetics. *Carbon* **2020**, *169*, 312−326.
(45) Reinert, L.; Zeiger, M.; Suárez, S.; Presser, V.; Mücklich, F. Dispersion analysis of carbon nanotubes, carbon onions, and nanodiamonds for their application as reinforcement phase in nickel metal matrix composites. *RSC Adv.* **2015**, *5*, 95149−95159.
(46) Washer, G.; Blum, F. Raman Spectroscopy for the Non-destructive Testing of Carbon Fiber. *Res. Lett. Mater. Sci.* **2008**, *2008*, 693207.
(47) Yao, D.; Zhang, Y.; Williams, P. T.; Yang, H.; Chen, H. Co-production of hydrogen and carbon nanotubes from real-world waste plastics: Influence of catalyst composition and operational parameters. *Appl. Catal., B* **2018**, *221*, 584−597.
(48) Streeter, I.; Wildgoose, G. G.; Shao, L.; Compton, R. G. Cyclic voltammetry on electrode surfaces covered with porous layers: An analysis of electron transfer kinetics at single-walled carbon nanotube modified electrodes. *Sens. Actuators, B* **2008**, *133*, 462−466.
(49) Gaolatlhe, L.; Barik, R.; Ray, S. C.; Ozoemena, K. I. Voltammetric responses of porous Co3O4 spinels supported on MOF-derived carbons: Effects of porous volume on dopamine diffusion processes. *J. Electroanal. Chem.* **2020**, *872*, No. 113863.
(50) Ozoemena, K. I.; Mathebula, N. S.; Pillay, J.; Toschi, G.; Verschoor, J. A. Electron transfer dynamics across self-assembled N-

https://doi.org/10.1021/acsomega.2c05722
ACS Omega 2022, 7, 47892−47905

(2-mercaptoethyl) octadecanamide/mycolic acid layers: impedimetric insights into the structural integrity and interaction with anti-mycolic acid antibodies. *Phys. Chem. Chem. Phys.* **2010**, *12*, 345−357.
(51) Pillay, J.; Ozoemena, K. I. Layer-by-layer self-assembled nanostructured phthalocyaninatoiron(II)/SWCNT-poly(m-amino-benzenesulfonic acid) hybrid system on gold surface: Electron transfer dynamics and amplification of H2O2 response. *Electrochim. Acta* **2009**, *54*, 5053−5059.
(52) Maxakato, N. W.; Arendse, C. J.; Ozoemena, K. I. Insights into the electro-oxidation of ethylene glycol at Pt/Ru nanocatalysts supported on MWCNTs: Adsorption-controlled electrode kinetics. *Electrochem. Commun.* **2009**, *11*, 534−537.
(53) Mofokeng, T. P.; Ipadeola, A. K.; Tetana, Z. N.; Ozoemena, K. I. Defect-Engineered Nanostructured Ni/MOF-Derived Carbons for an Efficient Aqueous Battery-Type Energy Storage Device. *ACS Omega* **2020**, *5*, 20461−20472.
(54) Orazem, M. E.; Tribollet, B.*Electrochemical Impedance Spectroscopy*; Wiley, 2017.
(55) Monk, P. M.*Fundamentals of Electroanalytical Chemistry*; John Wiley & Sons, 2008.
(56) Bard, A. J.; Faulkner, L. R.*Electrochemical Methods: Fundamentals and Applications*; Wiley, 2001.
(57) Compton, R. G.; Banks, C. E.*Understanding Voltammetry*; World Scientific, 2018.
(58) Ahmar, H.; Fakhari, A. R. Electro-oxidation and adsorptive stripping voltammetric determination of ephedrine and pseudoephedrine at carboxylated multi-walled carbon nanotube-modified electrode. *Anal. Methods* **2012**, *4*, 812−818.
(59) Zhang, J. T.; Tse, Y.-H.; Pietro, W. J.; Lever, A. B. P. Electrocatalytic activity of N,N',N″,N″-tetramethyl-tetra-3,4-pyridoporphyrazinocobalt(II) adsorbed on a graphite electrode towards the oxidation of hydrazine and hydroxylamine. *J. Electroanal. Chem.* **1996**, *406*, 203−211.
(60) Zagal, J. H. P.; Maritza, A. Electro-oxidation of hydrazine on electrodes modified with vitamin B12. *Electrochim. Acta* **1997**, *42*, 3477−3481.
(61) Siswana, M. P.; Ozoemena, K. I.; Nyokong, T. Electrocatalysis of asulam on cobalt phthalocyanine modified multi-walled carbon nanotubes immobilized on a basal plane pyrolytic graphite electrode. *Electrochim. Acta* **2006**, *52*, 114−122.
(62) Yang, T.; Yang, S.; Jin, W.; Zhang, Y.; Barsan, N.; Hemeryck, A.; Wageh, S.; Al-Ghamdi, A. A.; Liu, Y.; Zhou, J.; et al. Density Functional Investigation on alpha-MoO3 (100): Amines Adsorption and Surface Chemistry. *ACS Sens.* **2022**, *7*, 1213−1221.
(63) Wang, P.; Yuan, X.; Cui, Z.; Xu, C.; Sun, Z.; Li, J.; Liu, J.; Tian, Y.; Li, H. A Nanometer-Sized Graphite/Boron-Doped Diamond Electrochemical Sensor for Sensitive Detection of Acetaminophen. *ACS Omega* **2021**, *6*, 6326−6334.
(64) Nakhaee, S.; Hoyte, C.; Dart, R. C.; Askari, M.; Lamarine, R. J.; Mehrpour, O. A review on tramadol toxicity: mechanism of action, clinical presentation, and treatment. *Forensic Toxicol.* **2021**, *39*, 293−310.
(65) De Decker, K.; Cordonnier, J.; Jacobs, W.; Coucke, V.; Schepens, P.; Jorens, P. G. Fatal intoxication due to tramadol alone: case report and review of the literature. *Forensic Sci. Int.* **2008**, *175*, 79−82.
(66) Clarkson, J. E.; Lacy, J. M.; Fligner, C. L.; Thiersch, N.; Howard, J.; Harruff, R. C.; Logan, B. K. Tramadol (Ultram) concentrations in death investigation and impaired driving cases and their significance. *J. Forensic Sci.* **2004**, *49*, 2004019.
(67) De Backer, B.; Renardy, F.; Denooz, R.; Charlier, C. Quantification in postmortem blood and identification in urine of tramadol and its two main metabolites in two cases of lethal tramadol intoxication. *J. Anal. Toxicol.* **2010**, *34*, 599−604.
(68) Barbera, N.; Fisichella, M.; Bosco, A.; Indorato, F.; Spadaro, G.; Romano, G. A suicidal poisoning due to tramadol. A metabolic approach to death investigation. *J. Forensic Leg. Med.* **2013**, *20*, 555−558.

https://doi.org/10.1021/acsomega.2c05722
ACS Omega 2022, 7, 47892−47905